Potential for Energy Recovery of Unpowered Configurations Using Power Balance Method Computations

Ngonidzashe E. Mutangara,* Lelanie Smith,† and Kenneth J. Craig‡
University of Pretoria, Pretoria 0001, South Africa
and
Drewan S. Sanders §
Cranfield University, Bedford, England MK43 0AL, United Kingdom

*MEng Student, Department of Mechanical and Aeronautical Engineering; ngonidzashe.e.mutangara@cranfield.ac.uk. Student Member AIAA (Corresponding Author).
†Senior Lecturer, Department of Mechanical and Aeronautical Engineering; lelanie.smith@up.ac.za. Member AIAA.
‡Professor, Department of Mechanical and Aeronautical Engineering; ken.craig@up.ac.za.
§ Research Fellow, School of Aerospace, Transport and Manufacturing; d.s.sanders@cranfield.ac.uk. Member AIAA.

Abstract

New aircraft developments are made to improve aircraft performance and efficiency. One such method is integrating propulsion into the airframe. This allows for boundary-layer ingestion, which shows promise of significant power benefits. However, these benefits are difficult to quantify as the propulsion system and aircraft body become meticulously integrated. The thrust and drag are coupled and cannot be defined separately, making conventional performance analysis methods inapplicable. The power balance method (PBM) addresses this by quantifying aircraft performance in terms of mechanical flow power and change in kinetic-energy rate. The primary focus of this work was to perform computational studies implementing the PBM on unpowered aerodynamic bodies to evaluate their respective drag contributions. A secondary study was also conducted to quantify the energy recovery potential of various bodies using a potential for energy recovery factor. The computational fluid dynamics case studies showed that drag obtained using the PBM agreed to within 2% of conventional momentum-based approaches. Maximal energy recovery potential was consistently observed at the trailing ends of the geometries, with values ranging between 9 and 12%.

Nomenclature

A	=	area
CD	=	drag coefficient
C_p	=	pressure coefficient
D_F, L_F	=	body diameter and length
dS	=	surface element of control volume
dV	=	volume element of control volume
$\dot{E}_a$	=	axial kinetic-energy deposition rate
$\dot{E}_p$	=	pressure-work deposition rate
$\dot{E}_v$	=	transverse (vortex) kinetic-energy deposition rate
$\dot{E}_w$	=	lateral wave-outflow energy deposition rate
F_x	=	net streamwise force in x
M	=	Mach number
$\hat{\boldsymbol{n}}$	=	unit normal vector, out of control volume
P_K	=	net propulsor mechanical-energy inflow rate
P_S	=	net propulsor shaft power
P_V	=	volumetric mechanical power
p, p_t	=	static pressure and total pressure, respectively
Re	=	Reynolds number
u, v, w	=	perturbation velocities
$\mathcal{V}$	=	volume
$\boldsymbol{V}$	=	fluid velocity, $(V_\infty + u)\hat{x} + v\hat{y} + w\hat{z}$
V^2	=	fluid speed squared, which is equal to $\boldsymbol{V} \cdot \boldsymbol{V}$
V_n	=	side cylinder normal velocity $(vn_y + wn_z)$
W	=	aircraft weight
x, y, z	=	Cartesian axis coordinates
δ	=	boundary-layer thickness
$\dot{\mathcal{E}}$	=	mechanical-energy outflow rate
υ	=	kinematic viscosity
ρ	=	fluid density
τ	=	shear stress
$\bar{\boldsymbol{\tau}}$	=	viscous stress tensor
Φ	=	viscous-dissipation rate

Subscripts

ff	=	far-field quantity
m	=	recoverable mechanical-energy quantity
nf	=	near-field quantity
O	=	quantity on body surface
ref	=	reference quantity
TE	=	trailing-edge quantity
Φ	=	power balance quantity
∞	=	freestream quantity

Superscripts

SC	=	quantity on side cylinder
TP	=	quantity on transverse plane

I. Introduction

Aircraft performance assessment based on integral control volume (CV) analysis can broadly be categorized into force (momentum), kinetic (mechanical) energy, and exergy methods [1]. Momentum-based techniques include near-field integration, commonly used in most computational fluid dynamics (CFD) codes, calculating drag as the integration of stresses along the physical surfaces of the body. Another is the far-field method, which quantifies drag by analyzing flowfield perturbations. Near- and far-field methods are based on similar principles (i.e., momentum balance), but their analysis perspectives differ. The near-field approach focuses on the forces experienced by the body as a result of the flow passing over it. In contrast, far-field methods analyze flow disturbances, which occur as a result of the presence of a body within a flowfield. The near-field approach is limited in that it only allows for drag breakdown into friction and pressure components, whereas the far-field methods enable decompositions into more detailed, descriptive, and useful constituents. A variety of methods exist [2–7], allowing for aircraft forces to be calculated as a combination of surface [transverse plane (TP)¶] and/or volume integrals within the flow, based on expressions obtained from enthalpy and entropy relations.

Despite the advantages of these advanced methods, they are still reliant on thrust definitions for evaluating the efficacy of the propulsion system in terms of power requirements. The division between thrust and drag is a notional concept, and there is no clear inherent way of defining the useful (thrust) work done by the propulsion system [8]. For conventional configurations, there is "sufficient decoupling" between airframe and propulsion system aerodynamics, allowing for thrust definitions that approximate a valid, useful work for performance evaluation. However, where there is tighter integration between airframe and propulsion [as in the case of boundary-layer ingestion (BLI)], the aerocoupling does not allow for a valid distinction of useful work to be obtained from a definition of thrust power. Alternative methods attempt to overcome this challenge by expressing force decompositions within mechanical-energy [8,9] and exergy–anergy [10] conservation formulations. The underlying principle is to circumvent thrust-power-based performance evaluation by directly tracing power consumption development of different flow mechanisms within the flowfield. This enables a more holistic treatment of airframe–propulsion system performance evaluations.

Exergy–anergy formulations have shown to be particularly useful in providing complementary aerodynamic characteristic curves yielding a more complete aerodynamic assessment of aircraft configurations [11,12] and classical aerodynamic problems [13–16]. Aerodynamic analyses based on exergy are purely focused on a thermodynamic perspective, offering a clear distinction between reversible and irreversibly lost energy within a flowfield via an analysis of entropy, as shown by Aguirre et al. [16]. The authors of Refs. [10,11,17] further show that through its unique decomposition of drag, the recoverable energy within the airframe wake can be quantified. This is done through a figure of merit (FOM) known as the exergy waste coefficient (EWC), indicating the amount of energy available for utilization by BLI systems. Although opined as a more complete formulation due to its inclusion of the first and second laws of thermodynamics terms, for typical external aerodynamics applications that neglect heat transfer, exergy formulations effectively simplify to the power balance (PB) equation provided by Drela [9]. As energy-based methods focus on a mechanical-energy approach, they avoid the use of entropy terms, allowing for an improved physical interpretation of the decomposed force terms. Further to this, a factor similar to EWC exists based on mechanical-energy analysis known as the potential for energy recovery (PER)

introduced by Sanders and Laskaridis [8]. This presents an opportunity to analyze aerodynamic flows from a mechanical-energy perspective through these formulations, complementing prior work based on exergy via an alternative method of analysis.

The work in this paper focuses on the numerical implementation of the power balance method (PBM) on simple benchmark cases for verification within commercial CFD codes. Section II introduces the PBM, modified via a sequence of simplifications associated with unpowered configurations. Section III presents the case studies analyzed, split between flat plates and aerodynamic bodies, leading to the numerical verification and validation procedure in Sec. IV. Finally, in Sec. V, the drag over these geometries is reported using the PBM and compared against momentum-based approaches (i.e., near field and far field) for verification.

II. Mathematical Model

A. Momentum and Force Relations

Aerodynamic analysis using integral CV methods requires the definition of CVs around the aerodynamic body of interest, as shown in Fig. 1. The CV boundary *S* is partitioned into an inner boundary *SB* lying on the body surface and an outer boundary *SO* encapsulating the flowfield.

The profile drag over the body can be obtained either by computing the near-field on-body force $\boldsymbol{F}B$ or the outer-boundary force momentum flow $\boldsymbol{F}O$ via a sequence of integrals over the CV surfaces using Eqs. (1) and (2), provided by Drela [9]. These expressions describe how these forces are evaluated over aerodynamic bodies using near- and far-field approaches, respectively:

$$\boldsymbol{F}_B = \oiint [(p\hat{\boldsymbol{n}} - \bar{\boldsymbol{\tau}}) + \boldsymbol{V}\rho\boldsymbol{V}\cdot\hat{\boldsymbol{n}}]\,\mathrm{d}S_B \tag{1}$$

$$\boldsymbol{F}_O = \oiint -[(p - p_\infty)\hat{\boldsymbol{n}} + (\boldsymbol{V} - \boldsymbol{V}_\infty)\rho\boldsymbol{V}\cdot\hat{\boldsymbol{n}}]\,\mathrm{d}S_O \tag{2}$$

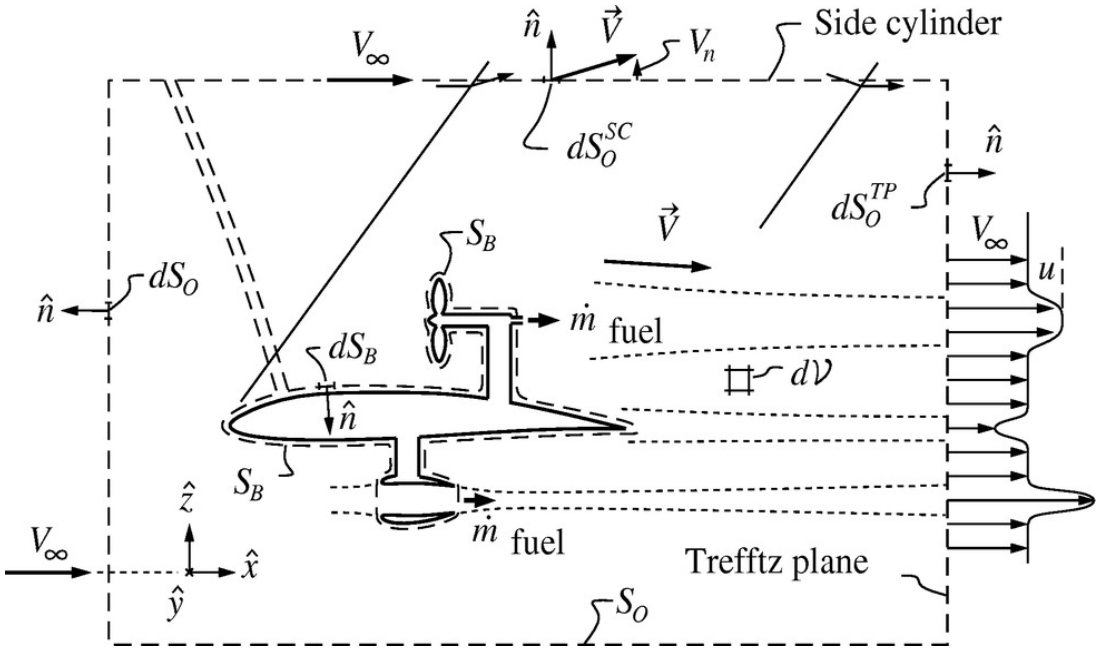

Fig. 1 Two-dimensional cutaway view of 3-D CV surrounding an aerodynamic body [9].

B. Mechanical-Energy Analysis

A mechanical-energy analysis of the body in Fig. 1 provides a prediction of the total flight power required through an estimation of the power outflow from various physical processes. It is, therefore, by the PB of the power outflow that the power inflow requirements can be obtained (i.e., $\dot{E}$inflow=$\dot{E}$outflow). Drela [9] expands this to give Eq. (3), which conveniently separates the power supplying and consuming processes on its left- and right-hand sides, respectively:

$$\underbrace{P_S + P_V + P_K}_{\text{Total power}} = \underbrace{\dot{\mathscr{E}}}_{\text{Total mechanical energy}} + \underbrace{\Phi}_{\text{Viscous dissipation}} \tag{3}$$

The method relies on the principle of conservation of mechanical energy, globally over the CV and locally within the wake [18]. The wake energy is defined as the sum of the mechanical energy deposited on the transverse plane (TP) (see footnote ¶) and the energy dissipated inside the wake region. This is then equated to the total power, given as the sum of the shaft *PS*, volumetric *PV*, and mechanical inflow power *PK* from the propulsors.

The total mechanical energy can be broken down further as done in Eq. (4), shown as the sum of the altitude potential energy, recoverable mechanical energy, and wave energy irreversibly lost to the surroundings:

$$\underbrace{\dot{\mathscr{E}}}_{\text{Total mechanical energy}} = \underbrace{W\dot{h}}_{\text{Altitude potential energy}} + \underbrace{\dot{E}_a + \dot{E}_v + \dot{E}_p}_{\text{Recoverable mechanical energy}} + \underbrace{\dot{E}_w}_{\text{Wave energy}} \tag{4}$$

C. Generalized Unpowered Analysis Simplifications

The analyses covered herein are restricted to unpowered bodies in steady flight; under these conditions, the altitude potential energy and drag power can be related through Eq. (5). By also considering the shaft and mechanical inflow power in Eq. (3) to be zero due to the absence of a propulsor, the remaining nonzero terms can be related to the drag power, as shown in Eq. (5). This equation is cast in a force decomposition format to allow a more straightforward evaluation of the body drag. The equation also highlights the recoverable and nonrecoverable components of the drag power for unpowered configurations; it is by the utilization of this recoverable energy that BLI obtains its benefits:

$$\underbrace{DV_\infty}_{\text{Drag power}} = -W\dot{h} = \underbrace{\dot{E}_a}_{\text{Axial wake energy}} + \underbrace{\dot{E}_v}_{\text{Transverse wake energy}} + \underbrace{\dot{E}_p}_{\text{Pressure-work rate}} + \underbrace{\dot{E}_w + \Phi}_{\text{Irreversibly lost energy}} - \underbrace{P_V}_{\text{Volumetric mechanical power}} \tag{5}$$

A nondimensional form of Eq. (5) can be obtained using the freestream dynamic pressure force power ($\frac{1}{2}\rho_\infty V_\infty^3 A_{\text{ref}}$). This nondimensionalization is directly comparable to the traditional drag coefficient [10], and a depiction of this process is shown in Eq. (6):

$$\text{CD} = \frac{D}{(1/2)\rho_\infty V_\infty^2 A_{\text{ref}}}; \qquad C\dot{E}_a = \frac{\dot{E}_a}{(1/2)\rho_\infty V_\infty^3 A_{\text{ref}}} \tag{6}$$

Lastly, further simplification of the PB formulation can be done when applied to inviscid flows. For this, viscous dissipation is neglected due to the absence of viscous effects.

D. BLI Performance Parameters

As the power saving coefficient [19] remains an FOM exclusively for powered configurations, Sanders and Laskaridis [8] introduce another FOM known as the PER. This factor evaluates the potential for aerodynamic improvement, similarly done by the EWC, through an analysis of the irreversibly lost energy at the body trailing edge. For subsonic flows, similar to those evaluated herein, irreversible losses arise mainly as a result of the viscous dissipation leading to a PER evaluation through Eq. (7):

$$\text{PER} = 1 - \frac{\Phi_{\text{TE}}}{DV_\infty} \tag{7}$$

Although intended for analysis at the airframe trailing edge, the analysis of PER can be extended further downstream, providing an additional assessment of the energies available for recovery for wake ingesting configurations. By so doing, a tacit link can be made between PER and EWC through a recasting of Eq. (7) by instead considering the recoverable energy outflow, as shown in Eq. (8). This new factor is simply a recasting and is equivalent to PER for incompressible flows; it will be referred to here as its complement (i.e., PER*c*). This then links the energy-based PER and exergy-based EWC when thermal and compressibility effects are negligible (typical for low-speed subsonic flows), as the formulations become approximately equivalent in this regard:

$$\mathrm{PER}^c = \frac{\dot{E}_a + \dot{E}_v + \dot{E}_p}{DV_\infty} = \frac{\text{Mechanical} - \text{energy outflow rate}}{\text{Drag power}} \approx \mathrm{EWC} \tag{8}$$

III. Numerical Methodology

A. Geometrical Model and Mesh Considerations

1. Inviscid, Laminar, and Turbulent Flat Plates

These analyses were modeled in commercial CFD code, STAR CCM+, in a 2-D structured mesh domain with no-slip wall boundaries (–) representing the flat plate (*LP*). The near-wall cells were arranged using a hyperbolic tangent distribution and a first-layer cell thickness of 0.1 mm to resolve the flat-plate boundary layer.

Figure 2a shows the mesh and boundary conditions for the extended flat-plate domain. The domain was extended a distance of one flat-plate length downstream of the trailing edge (indicated by the symmetry plane), allowing the wake to develop downstream. This was done to enable the PBM to quantify the wake-energy loss rates downstream of the flat plate. To ensure mesh independence, the grid-convergence index method [20] was used at different mesh refinement levels. The final mesh counts for the original (i.e., without the extended symmetry plane) and extended domains were 4×10^4 and 6×10^4, respectively.

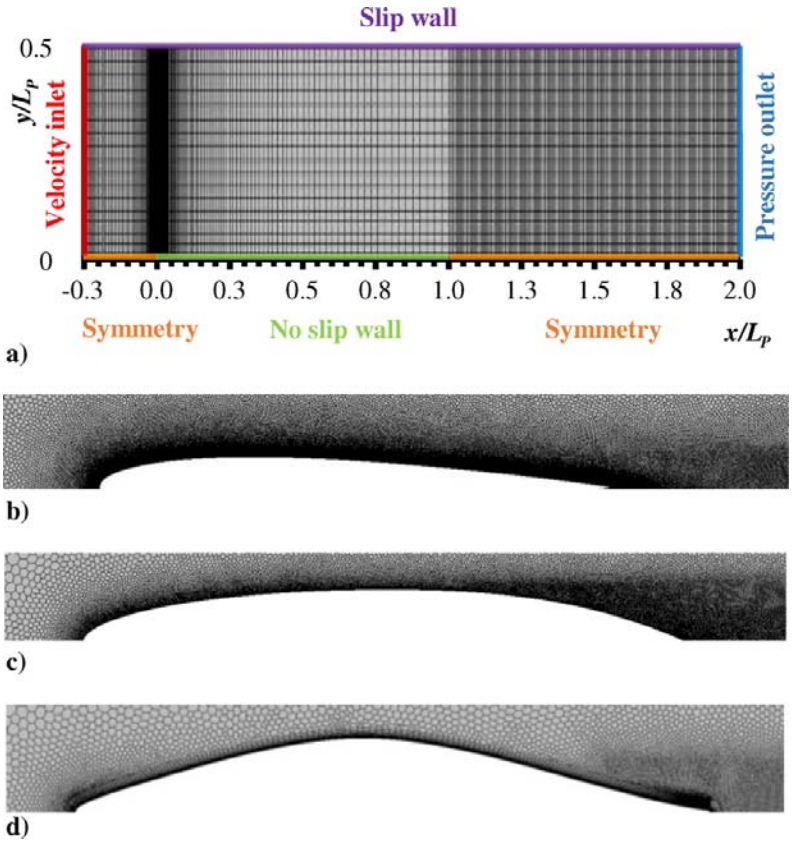

Fig. 2. Mesh representation around a) flat plate b) NACA 0012 airfoil c) MLDB and d) F-57 low drag body.

2. NACA 0012 Airfoil

The NACA 0012 airfoil was modeled as a 2-D body inside a circular computational flow domain, with a diameter of 16 chord lengths and an outer boundary assigned as freestream. The final mesh count for this study was approximately 6.7×10^5 cells created using unstructured polyhedral cells, as shown in Fig. 2b, with 15 prism layer cells used to resolve the boundary layer and yield a wall $y+$ near unity ($y+\approx1$). The resolution of the mesh was higher in regions where greater computational accuracy was needed, such as the airfoil surface and regions close to the airfoil trailing edge and wake.

3. Myring Low-Drag Body

The Myring low-drag body (MLDB) was modeled in a 2-D axisymmetric domain with the flow assumed as steady and incompressible. The domain consisted of a constant velocity inlet four body lengths upstream of the nose, specified to give a Reynolds number equal to the reference cases from the literature [21]. The outlet, located nine body lengths downstream of the trailing edge, was modeled as a pressure boundary set to atmospheric conditions, and the remaining outer boundary as a symmetry plane one body length from the axis line.

The mesh around the body, shown in Fig. 2c, was created using unstructured polyhedral cells with a nondimensional wall distance criterion kept less than unity ($y+<1$) (as required by the k–ω turbulence model). The final mesh count for this study was approximately 7.5×10^4 cells.

4. F-57 Low-Drag Body

The F-57 body was modeled using a half-section of the 3-D axisymmetric body and computational flow domain; this was done to reduce the computational cost by exploiting the flow symmetry. The computational domain consisted of wind-tunnel wall dimensions obtained from the experimental investigation by Patel and Lee [22]. Even though the walls were initially of octagonal cross section, simplification to a square cross section caused negligible deviation (<0.5%) on the force coefficient results [23].

Figure 2d shows the mesh around the F-57 body at $\alpha=0$ deg; volumetric refinements were employed to increase the mesh density in regions where viscous effects were prevalent (i.e., around the body and wake regions). The final mesh count obtained after refinement was approximately 5×10^6 cells. For compatibility with the turbulence model used and to accurately resolve the boundary layer, the maximum wall $y+$ distance was kept less than unity (i.e., $y+<1$).

B. Boundary Conditions, Turbulence, and Transition Models

1. Inviscid, Laminar, and Turbulent Flat Plates

The test cases analyzed were modeled as steady, ideal gas flow with a freestream inlet (–) $M\infty=0.2$ and pressure outlet boundaries set to atmospheric conditions. The symmetry boundary condition was used to represent the freestream approaching the flat plate. The length of the plate was given as $LP=2$ m at 0 deg angle of attack ($\alpha=0$ deg), yielding a Reynolds number based on the flat-plate length of 9×10^6.

The inviscid flow solutions were verified by comparison against an expected drag-coefficient solution of zero, which occurs due to the absence of both pressure and skin-friction drag. The laminar flow solutions were compared against the theoretical Blasius solution velocity and skin-friction coefficient profiles. For turbulent flow, the velocity profiles obtained using the shear-stress transport (SST) k–ω [24] and Spalart–Allmaras turbulence [25] models were compared against the inner, logarithmic, and Spalding's law of the wall for verification of the CFD code.

2. NACA 0012 Airfoil

The NACA 0012 airfoil boundary conditions were obtained from a numerical study conducted by Jespersen et al. [26]. The flow was assumed to be steady, incompressible, and fully turbulent, modeled using the Spalart–Allmaras turbulence model [25]. The chord length was given as 1 m (c=1 m), and the airfoil was kept at 0 deg angle of attack (α=0 deg). The freestream $M\infty$=0.15 resulted in a Reynolds number of 6×10^6 based on the airfoil chord.

3. Myring Low-Drag Body

The MLDB flow was assumed to be steady and incompressible (Re=$10^7$and $M\infty$=0.06), modeled using the SST k–ω turbulence model [24] coupled with the γ–$Re\theta$ transition model [27,28] to capture natural flow transition. To affirm the validity of the modeling conditions, the results were compared against numerical and theoretical data with the flow tripped at (x/LM=0.03), prescribed by Myring [21]. The tripped flow was modeled in STAR-CCM+ using the turbulence suppression (TS) model, which allowed turbulence effects to be neglected in specified regions.

4. F-57 Low-Drag Body

The F-57 body flow was assumed to be steady and incompressible ($M\infty$=0.04), with a constant velocity inlet condition of 15.24 m/s, and the body length was given as 1.219 m, yielding a Reynolds number based on body length of 1.2×10^6 obtained from experimental work by Patel and Lee [22]. The outlet pressure boundary was set to atmospheric conditions with the outer domains modeled as no-slip wall boundaries. The turbulence and transition models were selected as prescribed for aerospace application at low Reynolds number. The SST k–ω turbulence model [24] coupled with the γ–$Re\theta$ transition model [27,28] was used. The γ–$Re\theta$ transition model was required to predict the aerodynamic forces for flow physics involving laminar separation bubbles and flow transition. For validation, the results were compared against experimental work by Patel and Lee [22] with a tripped boundary layer at x/LF≈0.475.

IV. Comparison with Reference Cases

For the evaluation of drag over the geometries, two techniques based on momentum analysis introduced in Sec. II.A were considered as well as the PBM ($CD_{\Phi}^{\mathrm{Drela}}$) given in Eq. (3). To evaluate drag, the more straightforward near-field approach (CD*nf*) integrated the stresses over the body surface, whereas the far-field method (CD*ff*) relied on momentum balance across the CV outer boundary to obtain the on-body forces.

A. Inviscid, Laminar, and Turbulent Flat Plates

1. Inviscid Flat Plate

This section investigates the numerical implementation of the PBM postulated by Drela [9], for the analysis of inviscid flat plates. As a consequence of the flow being inviscid and at an angle of attack of 0 deg, neither pressure nor skin-friction drag is present, thus yielding a total drag-coefficient result of zero. This was confirmed by all the analysis method solutions being either equal to or approximately zero, as shown in Table 1, at the finest mesh resolution consisting of 2×10^4 cells.

Table 1. Two-dimensional flat plates in subsonic flow: near-field, far-field, and PB drag coefficients

Mesh refinement	Near-field CD_{nf}	Far-field CD_{ff}	PB CD_{Φ}^{Drela}
	Inviscid		
Fine	0	3.75×10^{-11}	5.69×10^{-13}
	Laminar		
Coarse	4.46×10^{-4}	4.57×10^{-4}	4.38×10^{-4}
Medium	4.48×10^{-4}	4.50×10^{-4}	4.42×10^{-4}
Fine	4.48×10^{-4}	4.50×10^{-4}	4.42×10^{-4}
	Turbulent		
Coarse	2.71×10^{-3}	2.75×10^{-3}	2.73×10^{-3}
Medium	2.77×10^{-3}	2.78×10^{-3}	2.76×10^{-3}
Fine	2.77×10^{-3}	2.78×10^{-3}	2.76×10^{-3}

2. Laminar Flat Plate

The study was extended to the remainder of the test cases, where the generalized unpowered simplification discussed in Sec. II.C was used. The volumetric mechanical power and wave-energy terms were also additionally dropped, as their influence is only expected to be significant for compressible (i.e., $M\infty>0.3$) and/or supersonic flows [9,29].

Figure 3a shows a comparison between the theoretical Blasius and numerical velocity profiles for the laminar flat plate. Overall, the numerical data showed good agreement with the theoretical, exhibiting small differences (<0.5%) at the finest grid refinement level. The small differences observed may be attributed to the fact that Blasius solution is derived for incompressible flow, whereas the test case was modeled as an ideal gas at $M\infty=0.2$, which, although minute, does exhibit temperature and density fluctuations.

The numerical skin-friction coefficient solutions were monitored and compared against the analytical expression whose profile was obtained from the numerical Blasius solution shown in Eq. (9):

$$C_f \approx \frac{0.664}{\sqrt{Re_x}} \tag{9}$$

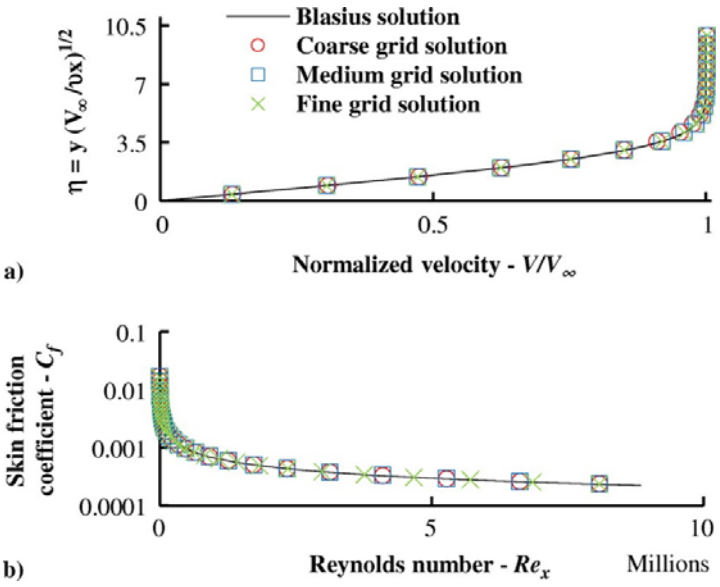

Fig. 3. Blasius solution and numerical a) velocity profile and b) skin-friction coefficient comparison at the flat-plate trailing edge for various mesh refinement levels.

At the finest grid refinement level, the numerical data were seen to closely match the analytical with negligible differences, as shown in Fig. 3b.

Table 1 summarizes the convergence behavior of the drag-coefficient solutions at various mesh refinement levels for the near-field method, far-field method, and PBM evaluated at the laminar flat-plate trailing edge. An increase in the mesh refinement level was shown to reduce the discrepancies of the far-field and PB solutions in comparison to the near-field alternative. A percentage difference of <2% was observed between the solutions at the finest mesh refinement level.

3. Turbulent Flat Plate

The prior laminar test case was extended to fully turbulent flow analyzed using the SST k–ω and Spalart–Allmaras turbulence models. This analysis focused on observing the behavior and performance of the PB formulation for turbulent flow regimes. Similar to the laminar flat plate, the numerical solutions were compared against analytical velocity profile distributions. Figure 4 shows this comparison, where the numerical, law of the wall, and Spalding's law [30] profiles are plotted. The Spalart–Allmaras model showed reasonable agreement with the theoretical profiles in both the viscous sublayer and logarithmic regions up to a log y+=2. The SST k–ω model performed similarly well in the viscous sublayer, but further from the wall, in the buffer and logarithmic regions, better agreement was obtained with Spalding's law (κ=0.4 and B=5.5).

Overall, the turbulent flat-plate drag coefficients summarized in Table 1 show good agreement with each other with the near-field, far-field, and PB solutions all showing differences <1%.

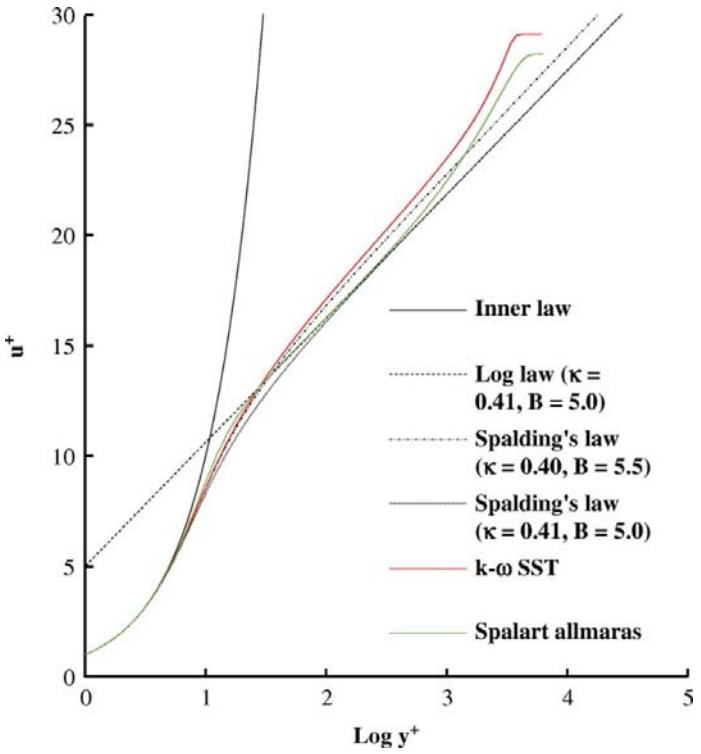

Fig. 4. Velocity profile comparison at x=1.9 m against the law of the wall and Spalding's law [30].

4. Turbulence Model Sensitivity Study

The influence of turbulence modeling on the performance of the PBM was investigated by a comparison of the SST k–ω and Spalart–Allmaras turbulence models. Particular interest was taken in the flow mechanisms, which helped explain any discrepancies produced by the turbulence models in their performance predictions. The results for the skin-friction coefficient distribution, as well as the numerical drag-coefficient data over the flat plate, were recorded to highlight the differences observed for each turbulence model.

Figure 5 shows the skin-friction coefficient profiles for the turbulence models and laminar flat plate, where the flow regime change (laminar to turbulent) resulted in a significant rise in skin friction. The profile differences observed between the SST k–ω and Spalart–Allmaras turbulence models may be attributed to the differences in turbulence model formulations and the respective near-wall treatments [31].

The increased skin friction for the Spalart–Allmaras model consequently then led to the higher total drag coefficient observed in Table 2. Additionally noted was a drag-coefficient difference of approximately 7% between the turbulence models. Regardless, the far-field method and PBM showed negligible difference (<1%) when compared against their respective near-field solutions.

Table 2. Two-dimensional flat plate: numerical drag coefficients for SST k − ω and Spalart–Allmaras turbulence models

Turbulence model	Near-field CD_{nf}	Far-field CD_{ff}	PB CD_{Φ}^{Drela}
SST *k–ω*	2.77×10^{-3}	2.78×10^{-3}	2.76×10^{-3}
Spalart–Allmaras	2.96×10^{-3}	2.97×10^{-3}	2.95×10^{-3}

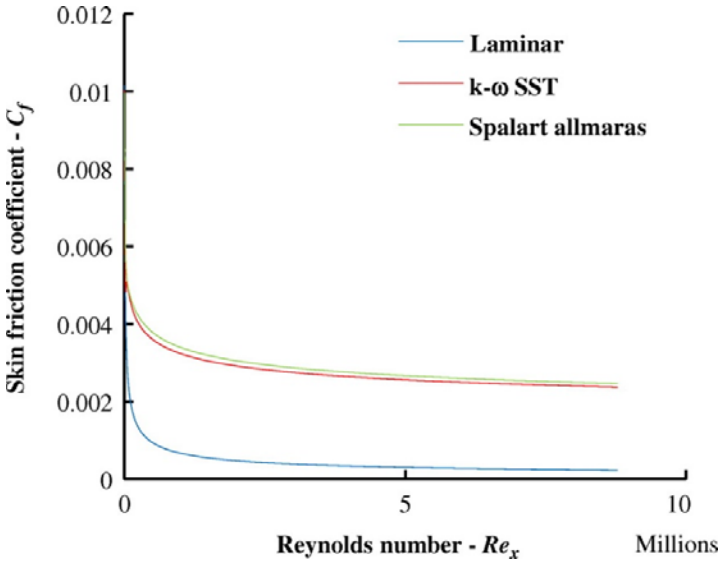

Fig. 5. Laminar and turbulent skin-friction coefficient profile comparison over the flat plate.

B. NACA 0012 Airfoil

The NACA 0012 airfoil numerical pressure coefficient profile was compared against experimental data provided by Gregory and O'Reilly [32] and Ladson [33] obtained at Re=3×10^6 and 6×10^6, respectively. The numerical results from the current study in Fig. 6a showed a similar general trend with the experimental and good agreement with the numerical data provided by Jespersen et al. [26]. Also shown in Fig. 6b is the skin-friction coefficient profile, which again showed close agreement with the data provided.

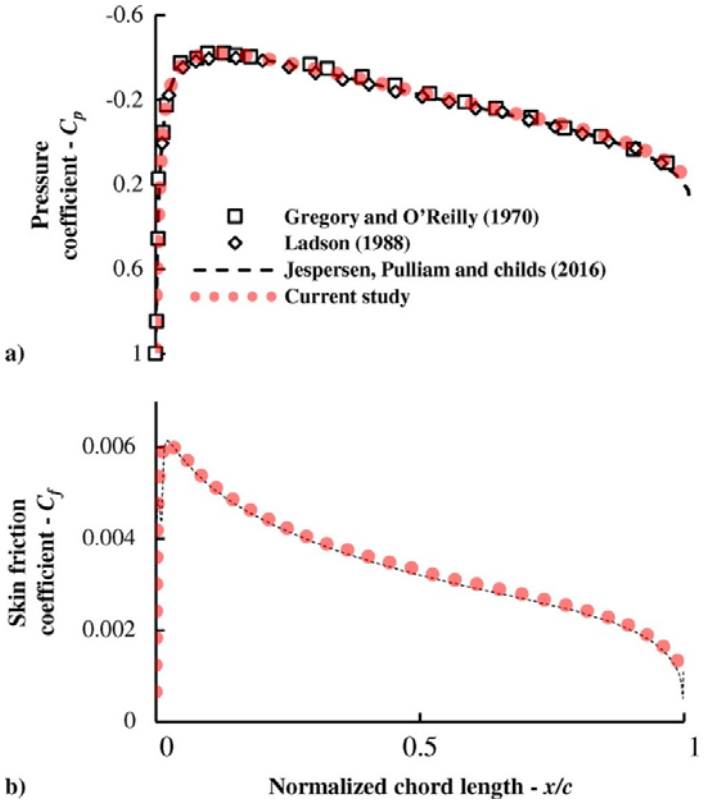

Fig. 6. NACA 0012 airfoil: a) pressure and b) skin friction coefficient data.

C. Myring Low-Drag Body

The numerical velocity distribution for the current study was compared against the analytical solution provided by Myring [21], showing good agreement with negligible differences between the distributions in Fig. 7. In comparison to the tripped flow scenario, the naturally transitioning flow resulted in the fluid accelerating further downstream before transition due to the positive velocity gradient, which extended up to approximately 70% of the body length. This yielded a natural transition location at $x/LM \approx 0.48$, further aft of the predicted, at $x/LM = 0.03$. The validity of these results was confirmed by their agreement with a similar study conducted by Smith et al. [23].

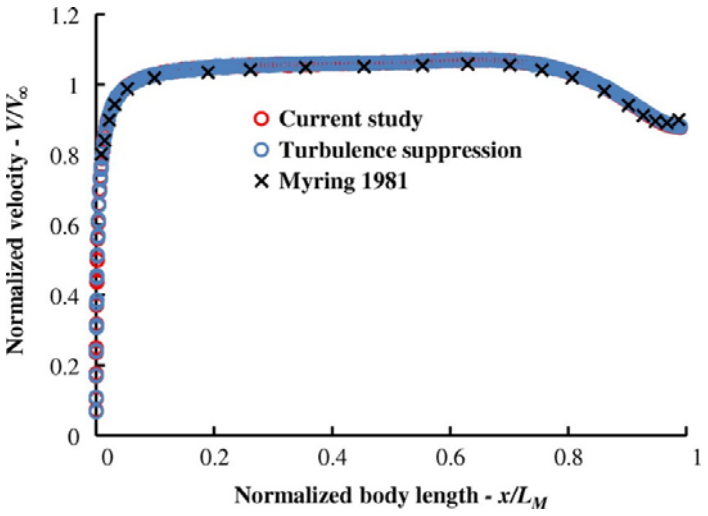

Fig. 7. Normalized velocity as a function of normalized body length for MLDB at $Re=10^7$.

D. F-57 Low-Drag Body

Figure 8a shows the numerically generated pressure coefficient *Cp* curve over the F-57 body in the normalized axial direction (i.e., x/LF), together with the experimental results of Patel and Lee [22]. The numerical data showed good agreement with the experimental data, with negligible *Cp* differences at the pressure probed experimental data points.

The pressure distribution around the body using the $\gamma-Re\theta$ transition model showed negligible differences in *Cp* compared to the TS model from $0 \leq x/LF \leq 0.475$. Patel and Lee [22] predicted this region as laminar flow before transition. As natural flow transition is allowed by the $\gamma-Re\theta$ transition model, a separation bubble was observed at $x/LF \approx 0.59$ indicated by the numerical departure in *Cp* at this location, which is in agreement with a similar study conducted by Smith et al. [23]. The numerical results return to showing negligible deviation in the distribution from $x/LF \approx 0.69$.

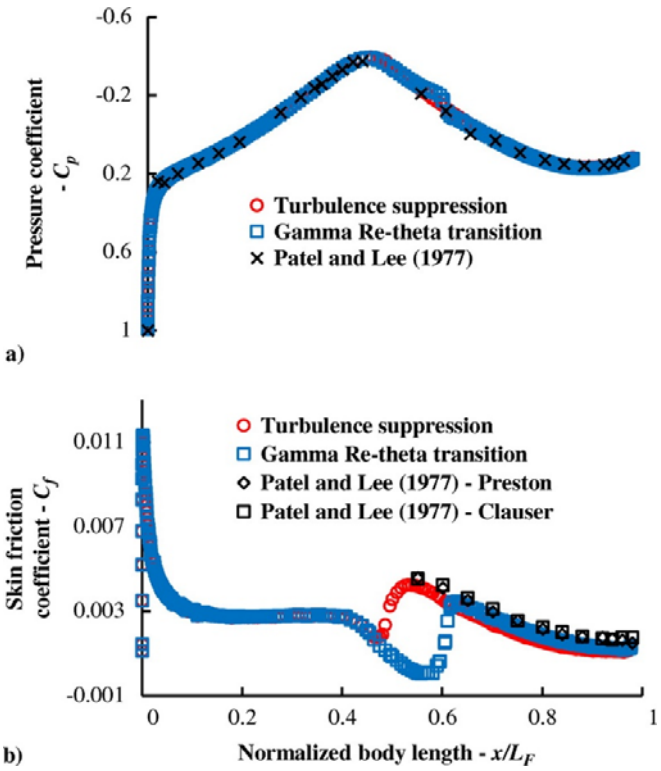

Fig 8. F-57 low-drag body: a) pressure coefficient and b) skin-friction coefficient as a function of normalized body length at Re=1.2×10^6.

Figure 8b shows the skin-friction coefficient over the body obtained by Patel and Lee [22] using Preston tubes; this method assumed the general law of the wall would remain valid for determining the wall shear stress over the body. An alternative approach suggested by Clauser [34] and modified using the extended law of the wall [35] is also shown. This method was used to correct the Preston tube data to determine the wall shear stress compatible with the wall.

The TS and γ–$Re\theta$ transition data showed the same general trend as the experimental, but tended to underpredict the magnitude of skin friction. This may likely have been due to the underprediction of turbulence anisotropy within the boundary layer, which is known to occur with the SST k–ω turbulence model [31].

The γ–$Re\theta$ transition data showed a higher (11% on average) skin-friction distribution in comparison with the TS data for regions x/LF>0.65 . The likely cause of this requires further investigation, but may be attributed to the modification of the boundary-layer profile due to natural flow transition, which, in contrast to the tripped flow case, allows the fluid to develop further downstream. The changes in the boundary-layer profile result in the modification of the skin-friction characteristics.

Figures 9a and 9b show the wake pressure coefficient and wake centerline velocity as a function of normalized body length. The numerical data from the TS and γ–$Re\theta$ transition models in Fig. 9a generally showed good agreement with the experimental data, except for an outlier located at x/LF=1.3.

The wake centerline velocity TS data in Fig. 9b also showed good agreement with the experimental with a maximum deviation of approximately 5%. The normalized velocity distribution for the γ–$Re\theta$ transition model, however, showed a much higher difference with a maximum of 12% at x/LF=1.4. The likely cause of this deviation can be attributed to the reduced turbulent kinetic-energy dissipation due to the flow transitioning further downstream in comparison with the tripped flow case, also mentioned by Smith et al. [36].

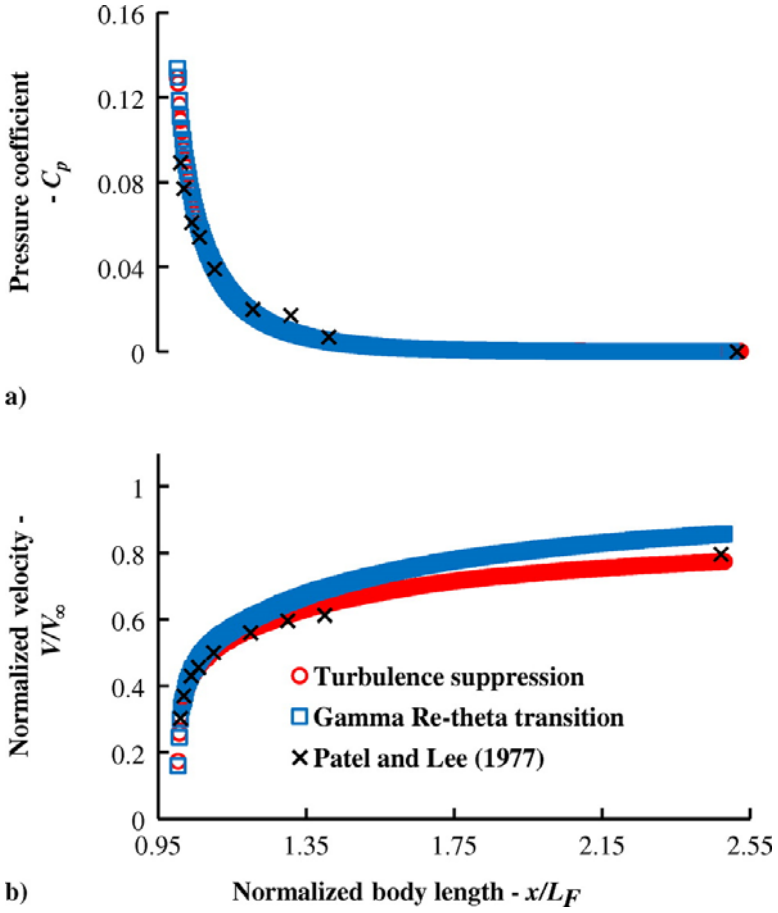

Fig. 9. F-57 low-drag body: a) wake pressure coefficient and b) normalized wake centerline velocity at Re=1.2×10^6.

V. Unpowered Configuration Wake-Energy Analysis

Drela [9] investigated the dependency of the PB terms on the transverse plane (TP) location. Drela mentioned that energy conservation ensures that the PB formulation holds for any side cylinder and TP location for a CV, provided the viscous dissipation Φ is defined to be within the CV [9]. Similar studies are conducted herein in terms of the nondimensionalized PB terms to assess the performance of this method when numerically implemented in commercial CFD code STAR CCM+. Of particular interest in this study was the mechanical-energy outflow rate $\dot{\varepsilon}m$, related to the streamwise and transverse kinetic-energy deposition rates ($\dot{E}a$ and $\dot{E}v$, respectively), as well as the pressure-defect work rate ($\dot{E}p$). The mechanical-energy outflow rate herein represents the amount of mechanical power available for BLI, where

$$\dot{\varepsilon}_m = \dot{E}_a + \dot{E}_v + \dot{E}_p \quad (10)$$

A. Laminar and Turbulent Flat Plates

1. Laminar Flat-Plate Wake-Energy Analyses at M∞*=0.20*

To quantify the energy loss rates within the wake, an analysis was conducted with a specific focus on the influence of the transverse plane (TP) location on the wake energy. Figure 10a shows the wake-energy variation of the PB terms as a function of the TP location. The TP was moved downstream of the flat-plate trailing edge a total distance of LP=2 m . The far-field and PB solutions are reported in Table 3 with their solutions given by their respective mean values and standard deviations, shown in brackets. The drag coefficients evaluated using the far-field method and PBM remained relatively constant as the TP progressively moved downstream, demonstrated by the small standard deviations reported in Table 3. This is in keeping with energy conservation, as explained by Drela [9]. Overall, the solutions showed negligible differences (<2%) when compared to the near-field solution.

Table 3. Extended domain laminar flat-plate numerical drag-coefficient results

	Mesh refinement (fine)
Near-field CD_{nf}	4.50×10^{-4}
Far-field CD_{ff}	4.51×10^{-4} ($\pm 1.03 \times 10^{-7}$)
PB CD_{Φ}^{Drela}	4.44×10^{-4} ($\pm 1.38 \times 10^{-7}$)

Additionally, the recoverable energy within the wake was found using the PER^c factor discussed in Sec. II.D through Eq. (8). Figure 10a shows the nondimensionalized contributions of the PB terms to the mechanical energy (denoted as $\dot{\varepsilon m}$), where the streamwise component ($\dot{CE a}$) showed the largest contribution. As the flat plate has no pressure gradient or curvature, contributions of $\dot{E p}$ and $\dot{E v}$ become negligible, leading to the flow being dominated by streamwise flow. Figure 10b shows the PERc percentage as a function of the TP location. Maximum recovery potential of ≈21% was observed at the flat-plate trailing edge, matching analytical solutions provided by Drela and Lv [9,37]. This recovery potential decreased downstream of the flat plate as the recoverable energy viscously dissipated.

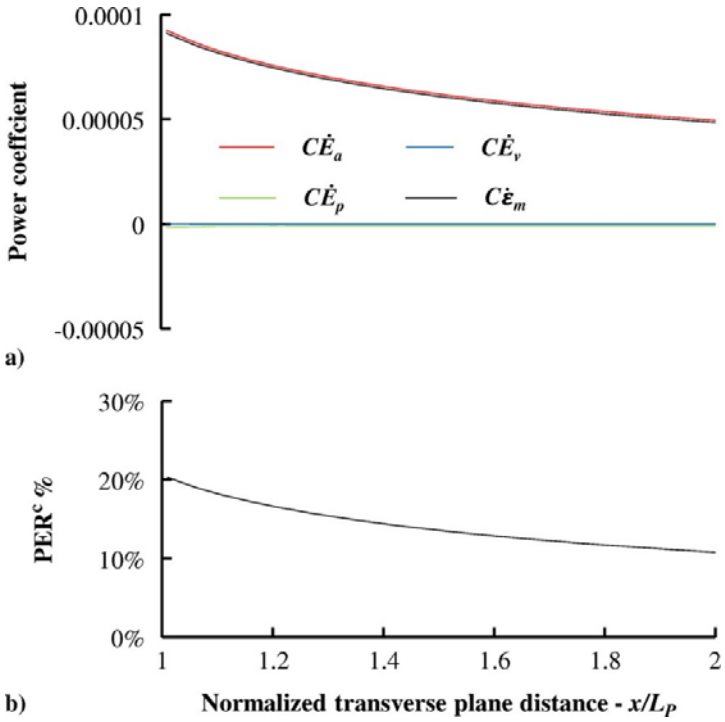

Fig. 10. Laminar flat plate: a) decomposition of the mechanical-energy outflow rate and b) recoverable energy in the wake at Re=9×10^6.

2. Turbulent Flat-Plate Wake-Energy Analyses at M∞*=0.20*

For the turbulent flat plate, a wake-energy analysis was conducted using the SST k–ω model. Additionally, a turbulence model sensitivity study was done, considering the performance of the Spalart–Allmaras model commonly used in aerospace applications.

The wake-energy analysis in Fig. 11a showed similar trends to those found in the laminar case study with the power sinks contributing highly to the total drag coefficient coming from the wake streamwise kinetic-energy deposition rate and viscous dissipation. The far-field method and PBM solutions reported in Table 4 again remained relatively constant when analyzed downstream of the trailing edge, showing good agreement with the near-field solution with a percentage difference of <1%.

Table 4. Extended domain turbulent flat-plate numerical drag-coefficient results

	Mesh refinement (fine)
Near-field CD_{nf}	2.78×10^{-3}
Far-field CD_{ff}	2.78×10^{-3} ($\pm 2.9 \times 10^{-6}$)
PB CD_{Φ}^{Drela}	2.76×10^{-3} ($\pm 6.8 \times 10^{-7}$)

The most significant recoverable energy contribution was observed again to come from the streamwise kinetic-energy deposition rate, as shown in Fig. 11a. In this instance, a maximum PER^c percentage of 9% was observed at the trailing edge, decreasing downstream to a value of 3% at x/LP=2, as shown in Fig. 11b.

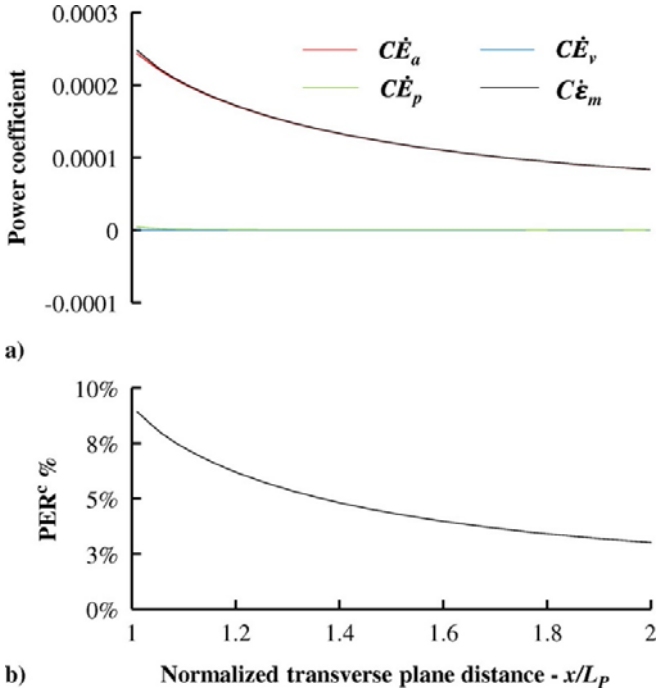

Fig. 11. Turbulent flat plate: a) decomposition of the mechanical-energy outflow rate and b) recoverable energy in the wake at Re=9×10^6.

As the laminar and turbulent case studies were analyzed using the same mesh and boundary conditions, inferences made from their solutions help to highlight the influence of the flow regime on wake energy. On comparing the two flowfields, an essential aspect is realized (i.e., the effects of turbulence on the recoverable wake energy).

Looking at Figs. 10 and 11, it can be seen that the amount of recoverable energy for laminar flow is considerably higher than that of the turbulent flow. The main reason for this being the higher viscous dissipation caused by the rise in skin friction for the turbulent flow in Fig. 5. The increased skin friction occurred as a result of the steeper velocity gradients and higher shear stresses near the wall of the turbulent flat plate. The higher viscous-dissipation contribution to the overall drag reduced the amount of recoverable energy in the wake, seen by the decreased PER^c percentage. Similarly, this can also be observed via an analysis of the velocity profiles of the different flow regimes, depicted in Fig. 12b. In the absolute reference frame shown in Fig. 12a, the flat plate moves through a stationary fluid where the area under its velocity profile represents the amount of kinetic energy imparted to a priorly stationary fluid. On comparing the laminar and turbulent profiles in Fig. 12b, it can be observed that the area under the turbulent profile is smaller than that of the laminar. This signifies that for the turbulent profile, the amount of kinetic energy imparted to the flow reduces instead, being viscously dissipated as heat and lost irreversibly to the surroundings.

As turbulent flow facilitates the transfer of mass, momentum, and energy within the boundary layer, this increases the shear stresses near the wall, leading to an increase in the drag coefficient when compared against the laminar flow case. Figure 13a shows the effect of the increased energy transfer within the boundary layer, which substantially increases the viscous dissipation.

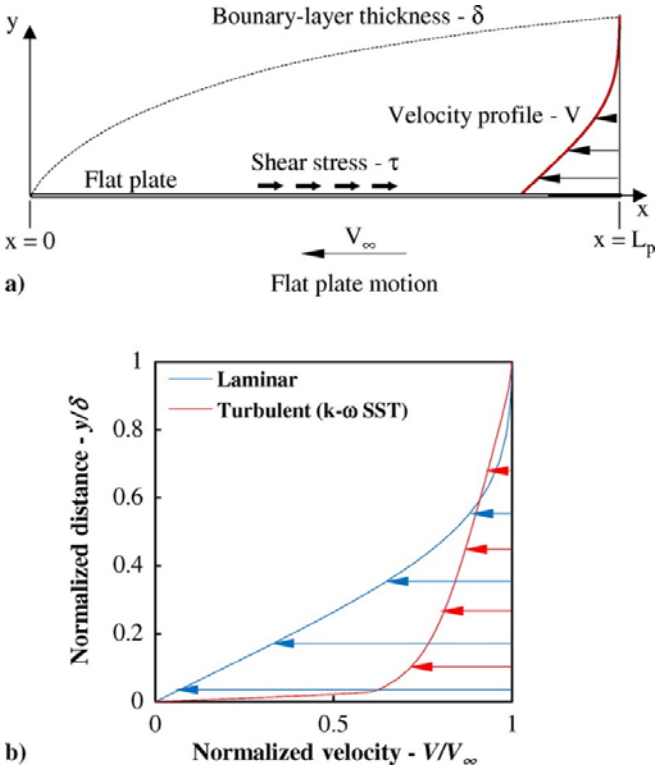

Fig. 12. Flat plate: a) absolute reference frame representation and b) velocity profile comparison at x=1.9 m for laminar and turbulent flows.

On comparison of the SST k–ω and Spalart–Allmaras turbulence models, reasonable agreement was observed between the wake streamwise energy profiles shown in Fig. 13a. The viscous dissipation obtained using the Spalart–Allmaras model, however, showed a noticeably higher distribution. The agreement between the wake streamwise energy profiles allowed for the higher skin-friction drag observed for the Spalart–Allmaras model to be loosely related to the viscous-dissipation quantity. This was somewhat expected, as one of the main differences between the turbulence models is their evaluation of turbulent viscosity, which plays a crucial role in the calculation of viscous dissipation. However, on comparison of the component contributions of the PB terms normalized by the drag power depicted in Fig. 13b, no significant differences between the turbulence model solutions were observed. This highlighted that, for this study, quantities, such as PER and PER^c, could be adequately evaluated using either turbulence model without any significant differences in the solution outcomes.

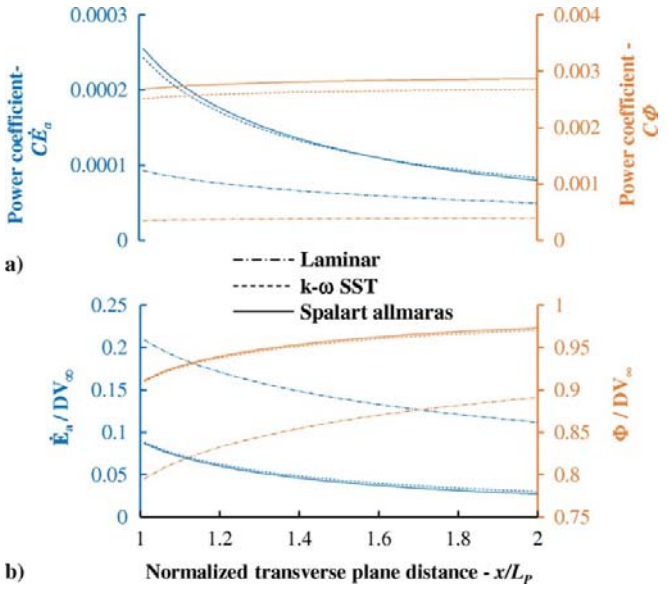

Fig. 13. Turbulence model comparison of a) axial wake kinetic energy and viscous-dissipation coefficients, and b) drag power normalized axial wake kinetic energy and viscous-dissipation rates.

B. NACA 0012 Airfoil

Figure 14a shows the wake-energy analysis of a NACA 0012 airfoil. The mechanical-energy outflow is seen to decay downstream of the body with the lost energy being viscously dissipated as heat. After one body length downstream, the mechanical-energy outflow reduces to the streamwise kinetic power as the contributions of the transverse and pressure-defect work rate decrease to zero.

The mechanical energy lost through the wake was quantified using the PER coefficients as done prior. Figure 14b shows the PER^c percentage as a function of the TP location; a maximum PER^c percentage of 12% was observed at the trailing edge with this value decaying downstream as the energy dissipated, yielding a value of 4% at x/c=2.

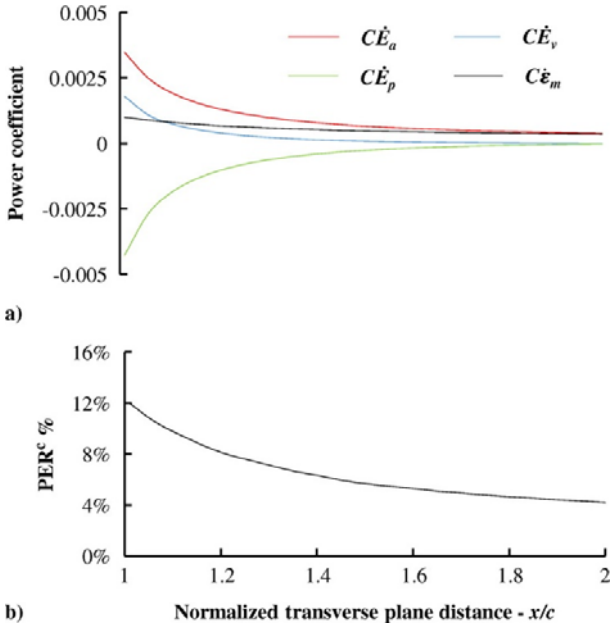

Fig. 14. NACA 0012 airfoil: a) decomposition of the mechanical-energy outflow rate and b) recoverable energy in the wake at Re=6×10^6.

The far-field and PB solutions in Table 5 were obtained at a TP located one body length downstream (i.e., x/c=2) where the solutions showed negligible difference (<1%) when compared against the near-field solution at the finest mesh refinement level.

Table 5. Two-dimensional NACA 0012 airfoil: near-field method, far-field method, and PBM drag coefficients

Mesh refinement	Near-field CD_{nf}	Far-field CD_{ff}	PB CD_{Φ}^{Drela}
Coarse	8.43×10^{-3}	8.47×10^{-3}	7.96×10^{-3}
Medium	8.36×10^{-3}	8.36×10^{-3}	8.18×10^{-3}
Fine	8.34×10^{-3}	8.33×10^{-3}	8.36×10^{-3}

C. Myring Low-Drag Body

Figure 15a shows the MLDB wake-energy analysis; the overall behavior of the terms is comparable to the NACA 0012 airfoil shown in Fig. 14a. Downstream of the trailing edge, the mechanical-energy outflow reduces to the streamwise kinetic energy as contributions from the transverse and pressure-defect work rate decrease to zero, also shown in Fig. 15a. Figure 15b provides the estimated PER^c percentage, which was observed to have a value of 11% at the body trailing end, gradually decaying downstream to approximately 5% at x/LM=2.

The drag-coefficient results reported in Table 6 are nondimensionalized in terms of body volume V, which is typical for bodies of revolution (BOR). The drag coefficients for BOR in this and the sections to follow will be nondimensionalized using Eq. (11):

$$\mathrm{CD} = \frac{D}{(1/2)\rho_\infty V_\infty^2 A_{\mathrm{ref}}}\left(\frac{A_{\mathrm{ref}}}{\mathscr{V}^{2/3}}\right); \qquad C\dot{E}_a = \frac{\dot{E}_a}{(1/2)\rho_\infty V_\infty^3 A_{\mathrm{ref}}}\left(\frac{A_{\mathrm{ref}}}{\mathscr{V}^{2/3}}\right) \tag{11}$$

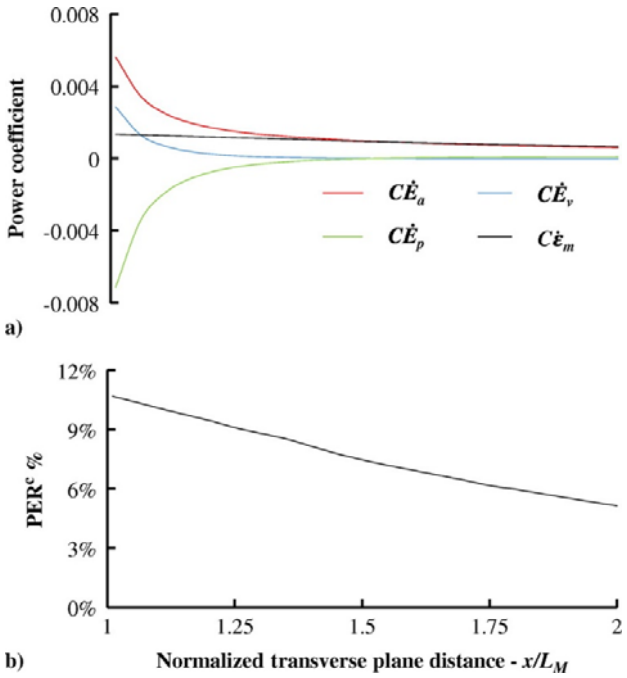

Fig. 15. Myring low-drag body: a) decomposition of the mechanical-energy outflow rate and b) recoverable energy in the wake at Re=10^7.

Table 6. Axisymmetric MLDB: near-field method, far-field method, and PBM volume-based drag coefficient

Mesh refinement	Near-field CD_{nf}	Far-field CD_{ff}	PB CD_{Φ}^{Drela}
Coarse	1.78×10^{-2}	1.83×10^{-2}	1.66×10^{-2}
Medium	1.26×10^{-2}	1.27×10^{-2}	1.25×10^{-2}
Fine	1.26×10^{-2}	1.27×10^{-2}	1.26×10^{-2}

Table 6 summarizes the drag-coefficient solutions for the near-field method, far-field method, and PBM. The far-field and PB solutions were obtained at a TP located one body length downstream of the MLDB, where their solutions were shown to be within <1% of the near-field value.

D. F-57 Low-Drag Body

Figure 16a shows the wake-energy analysis for the F-57 low-drag body; the trends observed in prior analyses for the NACA 0012 airfoil and MLDB with respect to the mechanical energy are also seen here. The mechanical-energy distribution is shown to decay gradually downstream until it matches the streamwise kinetic energy, which then becomes the main contributor to the overall mechanical energy. Figure 16b shows the wake energy available for recovery; a maximum PER^c percentage of 12% was observed at the body trailing end decaying downstream to approximately 5% at x/LF=2.

The drag over the body was analyzed using the far-field method and PBM, and compared to the near-field solution as done prior. At a TP located one body length downstream, the solutions from the far-field method and PBM were seen to show agreement with the near-field solution to within <2% , as shown in Table 7.

Table 7. F-57 low-drag body: near-field, far-field, and PB volume-based drag coefficients

Mesh refinement	Near-field CD_{nf}	Far-field CD_{ff}	PB CD_{Φ}^{Drela}
Coarse	1.66×10^{-2}	1.66×10^{-2}	1.59×10^{-2}
Medium	1.65×10^{-2}	1.66×10^{-2}	1.61×10^{-2}
Fine	1.65×10^{-2}	1.66×10^{-2}	1.62×10^{-2}
Very fine	1.65×10^{-2}	1.66×10^{-2}	1.62×10^{-2}

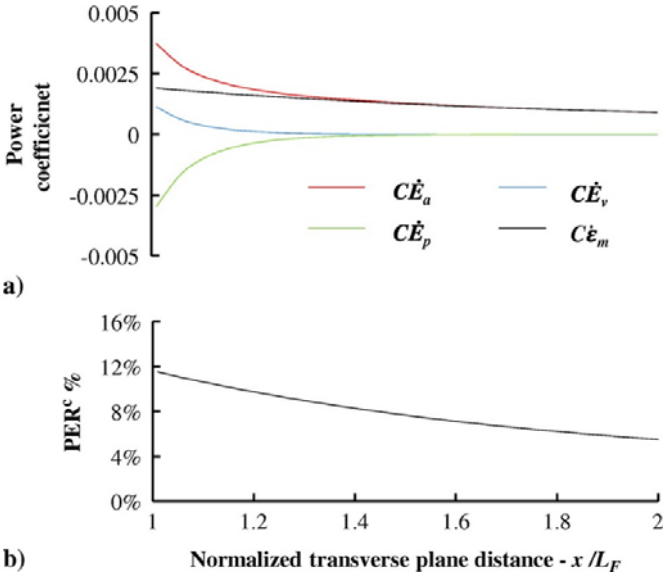

Fig. 16. a) Decomposition of the mechanical-energy outflow rate and b) F-57 low-drag body recoverable energy in the wake at Re=1.2×10^6.

VI. Discussion of Results

The PER^c performance of the various bodies was compared using the solutions obtained in the prior sections. The laminar flat-plate results, shown in Fig. 17a, provided an upper limit for PER^c with a value of 21% based on Blasius solution, whereas the turbulent flat plate gave the lower limit of 9%. The decrease in PER^c for the turbulent flat plate occurred as a result of the increased viscous losses caused by the higher shear stresses near the flat-plate wall. The effect of increasing Reynolds number yielded a similar outcome, with less kinetic energy being imparted to the flow and instead being viscously dissipated as heat to the surroundings. This was clearly shown in comparison of the fully turbulent NACA 0012 airfoil and flat plate, where the decrease in PER^c observed for the higher-Reynolds-number turbulent flat plate was accompanied by an increase in viscous dissipation, as depicted in Fig. 17b.

From these observations, it would be expected that the MLDB, being at the highest Reynolds number of 10^7 , would yield the lowest PER^c and highest viscous-dissipation component relative to its drag power. However, on analysis, a PER^c of 11% was obtained, much higher than expected for this Reynolds number. This occurred as a result of the body having significant regions of natural laminar flow with a transition location at x/LM≈0.48. As a result, the benefits of natural laminar flow could be realized, resulting in a PER^c and viscous-

dissipation component comparable to that of the lowest-Reynolds-number F-57 case study, as shown in Figs. 17a and 17b.

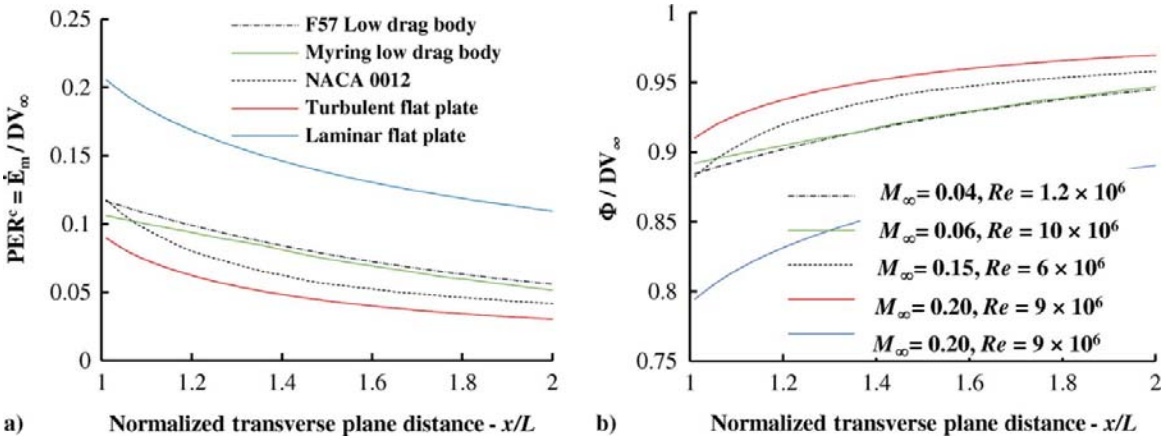

Fig. 17. Test case Reynolds and Mach number comparisons for a) PER^c and b) drag power normalized viscous dissipation rate.

Although the F-57 low-drag body was analyzed at the most favorable Reynolds number with regard to PER^c , its aftbody flow was not desirable. The strong pressure gradient and laminar separation bubble observed in this region resulted in lower energy recovery potential at its trailing edge. Therefore, from this, it is opined that to increase the energy recovery potential of a body, careful consideration must be taken with regard to the surface curvature, focusing mainly on using the benefits of natural laminar flow while avoiding strong pressure gradients and separation.

VII. Conclusions

The PBM decomposition of the various mechanisms contributing toward airframe drag provided a more in-depth description compared to the usual sum of pressure and skin-friction drag components. This allowed for a unique grouping of components into nonrecoverable and recoverable energy sources, which becomes of particular interest for BLI.

The flat-plate case studies identified the differences between laminar and turbulent flows with respect to the amount of recoverable energy available for BLI. The laminar flat plate showed a higher energy recovery potential for BLI (i.e., PER^c percentage=21%) in comparison to turbulent flow (i.e., PER^cpercentage=9%). This was observed due to the fact that laminar flow loses less energy irreversibly to the surroundings, following from the reduced influence of skin friction.

The turbulent flat-plate case studies also compared the Spalart–Allmaras and SST k–ω turbulence models with respect to their drag coefficients using near-field method, far-field method, and PBM. The study showed that even though the two turbulence model drag coefficients differed by approximately 7%, the drag prediction performances of the PBM and far-field method were unaffected, with their results still showing good agreement with their respective near-field solutions.

The final case studies focused on numerically verifying the PBM drag decompositions on a 2-D NACA 0012 airfoil at Re=6×10^6 , a 2-D axisymmetric body of revolution (MLDB) at Re=10^7, and a 3-D BOR with a strong pressure gradient at Re=1.2×10^6. The analyses consistently showed that the results for all three methods (near field, far field, and PB) were in close agreement to within 2%, increasing the reliability of the solutions due to the cross-validation procedure. As expected, the bodies all showed maximal recovery potential at their trailing ends, with the NACA 0012 airfoil and F-57 low-drag body yielding PER^c percentages of 12 and 11% for the MLDB. The PER^c performance of the transitional flow MLDB highlighted the importance of surface topology in increasing the recovery potential, specifically by using the benefits of natural laminar flow, which reduces the irreversible losses.

¶ The transverse plane represents an integration plane which becomes analogous to the Trefftz plane when located sufficiently far downstream.

Acknowledgments

The authors would like to thank the University of Pretoria Department of Research and Innovation as well as Cranfield School of Aerospace, Transport and Manufacturing for their support and funding during the development of this work.

References

[1] Habermann, A. L., Bijewitz, J., Seitz, A., and Hornung, M., "Performance Bookkeeping for Aircraft Configurations with Fuselage Wake-Filling Propulsion Integration," CEAS Aeronautical Journal, Vol. 11, June 2020, pp. 529–551. https://doi.org/10.1007/s13272-019-00434-w

[2] Giles, M. B., and Cummings, R. M., "Wake Integration for Three-Dimensional Flowfield Computations: Theoretical Development,"Journal of Aircraft, Vol. 36, No. 2, 1999, pp. 357–365. https://doi.org/10.2514/2.2465

[3] Paparone, L., and Tognaccini, R., "Computational Fluid Dynamics-Based Drag Prediction and Decomposition," AIAA Journal, Vol. 41, No. 9, 2003, pp. 1647–1657. https://doi.org/10.2514/2.7300

[4] Mele, B., Ostieri, M., and Tognaccini, R., "Aircraft Lift and Drag Decomposition in Transonic Flows," Journal of Aircraft, Vol. 54, No. 5, 2017, pp. 1933–1944. https://doi.org/10.2514/1.C034288

[5] Destarac, D., and van der Vooren, J., "Drag/Thrust Analysis of Jet-Propelled Transonic Transport Aircraft; Definition of Physical Drag Components," Aerospace Science and Technology, Vol. 8, No. 6, 2004, pp. 545–556. https://doi.org/10.1016/j.ast.2004.03.004

[6] Yamazaki, W., Matsushima, K., and Nakahashi, K., "Drag Prediction, Decomposition and Visualization in Unstructured Mesh CFD Solver of TAS-Code," International Journal for Numerical Methods in Fluids, Vol. 57, No. 4, 2008, pp. 417–436. https://doi.org/10.1002/fld.1643

[7] Yamazaki, W., Matsushima, K., and Nakahashi, K., "Aerodynamic Design Optimization Using the Drag-Decomposition Method," AIAA Journal, Vol. 46, No. 5, 2008, pp. 1096–1106. https://doi.org/10.2514/1.30342

[8] Sanders, D. S., and Laskaridis, P., "Full-Aircraft Energy-Based Force Decomposition Applied to Boundary-Layer Ingestion," AIAA Journal, Vol. 58, No. 10, 2020, pp. 4357–4373. https://doi.org/10.2514/1.J058695

[9] Drela, M., "Power Balance in Aerodynamic Flows," AIAA Journal, Vol. 47, No. 7, 2009, pp. 1761–1771. https://doi.org/10.2514/1.42409.

[10] Arntz, A., "Civil Aircraft Aero-Thermo-Propulsive Performance Assessment by an Exergy Analysis of High-Fidelity CFD-RANS Flow Solutions," Ph.D. Dissertation, Université de Lille, Lille, France, 2014.
[11] Arntz, A., and Atinault, O., "Exergy-Based Performance Assessment of a Blended Wing–Body with Boundary-Layer Ingestion," AIAA Journal, Vol. 53, No. 12, 2015, pp. 3766–3776. https://doi.org/10.2514/1.J054072
[12] Arntz, A., and Hue, D., "Exergy-Based Performance Assessment of the NASA Common Research Model," AIAA Journal, Vol. 54, No. 1, 2016, pp. 88–100. https://doi.org/10.2514/1.J054127
[13] Aguirre, M. A., and Duplaa, S., "Exergetic Drag Characteristic Curves," AIAA Journal, Vol. 57, No. 7, 2019, pp. 2746–2757. https://doi.org/10.2514/1.J057985
[14] Aguirre, M. A., Duplaa, S., and Carbonneau, X., "2D Flow Field Analysis by the Exergetic Method," AIAA Aviation 2019 Forum, AIAA Paper 2019-2925, June 2019. https://doi.org/10.2514/6.2019-2925
[15] Aguirre, M., Duplaa, S., and Carbonneau, X., "Vortex Exergy Prediction," 54th 3AF International Conference on Applied Aerodynamics, Paris, France, 2019, pp. 1–10.
[16] Aguirre, M., Duplaa, S., Carbonneau, X., and Turnbull, A., "A Systematic Analysis of the Mechanical Exergy of an Airfoil by Using Potential Flow, Euler & RANS," 24ème Congrès Français de Mécanique, Courbevoie, France, 2019, pp. 1–22.
[17] Arntz, A., Atinault, O., Destarac, D., and Merlen, A., "Exergy-Based Aircraft Aeropropulsive Performance Assessment: CFD Application to Boundary Layer Ingestion," 32nd AIAA Applied Aerodynamics Conference, AIAA Paper 2014-2573, June 2014. https://doi.org/10.2514/6.2014-2573
[18] Arvind, R., and Peijian, L., "Conceptual Analysis of Boundary Layer Ingestion Towards Propulsion Integration," Proceedings of the International Society of Air Breathing Engines (ISABE), Indianapolis, IN, 2013, pp. 1–15.
[19] Smith, L. H., "Wake Ingestion Propulsion Benefit," Journal of Propulsion and Power, Vol. 9, No. 1, 1993, pp. 74–82. https://doi.org/10.2514/3.11487
[20] Anon., Standard for Verification and Validation in Computational Fluid Dynamics and Heat Transfer, V&V 20, American Soc. of Mechanical Engineers, New York, 2009, pp. 11–14.
[21] Myring, D. F., "A Theoretical Study of the Effects of Body Shape and Mach Number on the Drag of Bodies of Revolution in Subcritical Axisymmetric Flow," Royal Aircraft Establishment TR 81005, Farnborough, Hants, U.K., 1981.
[22] Patel, V. C., and Lee, Y. T., "Thick Axisymmetric Turbulent Boundary Layer and Near Wake of a Low-Drag Body of Revolution," Inst. of Hydraulic Research Rept. 210, Univ. of Iowa, Iowa City, IA, 1977.
[23] Smith, L., Craig, K. J., Meyer, J. P., and Spedding, G. R., "Modifying Low-Drag Bodies to Generate Lift: A Computational Study," Journal of Aircraft, Vol. 54, No. 3, 2017, pp. 1150–1161. https://doi.org/10.2514/1.C034051
[24] Menter, F. R., "Two-Equation Eddy-Viscosity Turbulence Models for Engineering Applications," AIAA Journal, Vol. 32, No. 8, 1994, pp. 1598–1605. https://doi.org/10.2514/3.12149
[25] Spalart, P., and Allmaras, S., "A One-Equation Turbulence Model for Aerodynamic Flows," 30th Aerospace Sciences Meeting and Exhibit, AIAA Paper 1992-0439, Jan. 1992. https://doi.org/10.2514/6.1992-439
[26] Jespersen, D. C., Pulliam, T. H., and Childs, M. L., "OVERFLOW Turbulence Modeling Resource Validation Results," NAS TRNAS-2016-01, 2016.
[27] Menter, F. R., Langtry, R. B., Likki, S. R., Suzen, Y. B., Huang, P. G., and Völker, S., "A Correlation-Based Transition Model Using Local Variables Part I: Model Formulation,"

Proceedings of the ASME Turbo Expo 2004, Vol. 4, American Soc. of Mechanical Engineers, New York, 2004, pp. 57–67. https://doi.org/10.1115/GT2004-53452
[28] Langtry, R. B., Menter, F. R., Likki, S. R., Suzen, Y. B., Huang, P. G., and Völker, S., "A Correlation-Based Transition Model Using Local Variables—Part II: Test Cases and Industrial Applications," Journal of Turbomachinery, Vol. 128, No. 3, 2006, pp. 423–434. https://doi.org/10.1115/1.2184353
[29] Uranga, A., Drela, M., Hall, D. K., and Greitzer, E. M., "Analysis of the Aerodynamic Benefit from Boundary Layer Ingestion for Transport Aircraft," AIAA Journal, Vol. 56, No. 11, 2018, pp. 4271–4281. https://doi.org/10.2514/1.J056781
[30] Spalding, D. B., "A Single Formula for the 'Law of the Wall'," Journal of Applied Mechanics, Vol. 28, No. 3, 1961, pp. 455–458. https://doi.org/10.1115/1.3641728
[31] Anon., Simcenter STAR-CCM+® Documentation, CD-adapco, Melville, NY, 2019, pp. 3657–3834, 7094–7197.
[32] Gregory, N., and O'Reilly, C. L., "Low-Speed Aerodynamic Characteristics of NACA 0012 Aerofoil Section," Ministry of Defence Aeronautical Research Council R&M No. 3726, 1970.
[33] Ladson, C. L., "Effects of Independent Variation of Mach and Reynolds Numbers on the Low-Speed Aerodynamic Characteristics of the NACA 0012 Airfoil Section," NASA Langley Research Center TM-4074, 1988.
[34] Clauser, F. H., The Turbulent Boundary Layer, edited by H. L. Dryden, nd T. von Kármán, Elsevier, 1956, pp. 1–51. https://doi.org/10.1016/S0065-2156(08)70370-3
[35] Patel, V. C., "A Unified View of the Law of the Wall Using Mixing-Length Theory," Aeronautical Quarterly, Vol. 24, No. 1, 1973, pp. 55–70. https://doi.org/10.1017/S0001925900006429
[36] Smith, L., Davis, T. W., Spedding, G., and Meyer, J. P., "Numerical and Laboratory Experiments on a New Wing-Body-Tail Configuration," 54th AIAA Aerospace Sciences Meeting, AIAA Paper 2016-0800, Jan. 2016. https://doi.org/10.2514/6.2016-0800
[37] Lv, L., "Theoretical and Experimental Investigation of Boundary Layer Ingestion for Aircraft Application," Ph.D. Thesis, Delft University of Technology, Delft, The Netherlands, 2019.